Kinetics of structure formation in the vicinity of the glass transition

Acta Materialia 226 (2022) 117630

Contents lists available at ScienceDirect

Acta Materialia

journal homepage: www.elsevier.com/locate/actamat

Full length article

Kinetics of structure formation in the vicinity of the glass transition

Jürgen E.K. Schawe[a,b], Jörg F. Löffler[a,*]

[a] Laboratory of Metal Physics and Technology, Department of Materials, ETH Zurich, 8093 Zurich, Switzerland
[b] Mettler-Toledo GmbH, Analytical, 8606 Nänikon, Switzerland

ARTICLE INFO

Article history:
Received 5 August 2021
Revised 5 January 2022
Accepted 5 January 2022
Available online 7 January 2022

Keywords:
Glass stability
Ultrafast calorimetry
Metallic glass
Kinetics
Nucleation and crystallization

ABSTRACT

The structural stability of a gold-based bulk metallic glass ($Au_{49}Ag_{5.5}Pd_{2.3}Cu_{26.9}Si_{16.3}$) was investigated by fast differential scanning calorimetry (FDSC). A chemically homogeneous glass (CHG) containing no quenched-in nuclei was produced using sufficiently fast cooling from the melt. To characterize the stability of this glass, the structural variations during annealing in the glassy state were investigated and a sequence of five different events observed. These are structural relaxation, an incubation period, nucleation, crystallization, and finally reorganization. The kinetics of these processes and the stability of the crystalline structures are discussed.

1. Introduction

The glass-forming ability (GFA) characterizes the minimum conditions that must be fulfilled to create a glass by cooling from the melt. For the quantitative description of GFA many empirical approaches have been suggested, considering different characteristic transformation temperatures [1–5]. A more straightforward approach for characterizing GFA is the critical cooling rate, $\beta_{c,crit}$, at which the crystallization is bypassed during cooling and, as a result, a glass is formed below the glass transition temperature, T_g [6–9]. The critical cooling rate of bulk metallic glass (BMG)-forming alloys and the time–temperature–transformation (TTT) diagram can be directly measured by fast differential scanning calorimetry (FDSC) [9–12]. Due to the high possible cooling rates, FDSC can be also used to generate glasses with a high fictive temperature [13] and accelerated structural relaxation [14]. This enabled the study of relaxation kinetics in a wide time and temperature range.

The critical heating rate, $\beta_{h,crit}$, is another property, which describes the stability of the supercooled liquid. This is the minimum heating rate at which no crystallization occurs during heating from the glassy state to the melt. The lower $\beta_{h,crit}$, the lower is the tendency of the supercooled melt to crystallize. The critical heating rate depends on the number of quenched-in nuclei and the nucleation rate during heating. For conventionally quenched metallic glasses, $|\beta_{c,crit}| << \beta_{h,crit}$ [11,15,16], which indicates the existence of quenched-in nuclei that have formed during the previous cooling process.

A detailed investigation into the influence of cooling rate on the crystallization behavior of metallic glass during heating has revealed the existence of two different kinds of glass: (1) A chemically homogeneous glass (CHG), which is a monolithic glass that does not contain nuclei, and (2) a self-doped glass (SDG), which includes quenched-in nuclei formed during melt cooling [17]. The critical cooling rate to form a CHG is much higher than that to produce a SDG. The critical heating rate to bypass crystallization during heating from the glass, however, is lower for CHG than for SDG.

The thermal stability of a glass is related to the kinetics of structural relaxation, nucleation and crystal growth in the (partially) vitrified state [18]. Using "Tammann's nuclei development approach" [19], Schick, Androsch and co-workers [20–22] have shown for various partially crystalline polymers that three successive and coupled processes occur after rapid cooling and tempering in the glassy state. These are (i) complete structural relaxation, (ii) nucleation, and (iii) crystallization. Such a pathway of structural development has also been found recently in organic materials [23], a Ce-based BMG [24], and selenium [25].

Deviating behavior has been observed in low-molecular-weight organic materials at annealing far below the glass transition, where crystallization occurred before structural relaxation completed [26]. Chemically confined statistical copolymers also behave differently, and in such materials structural relaxation and crystallization have been shown to reveal the same kinetics [27].

* Corresponding author.
E-mail address: joerg.loeffler@mat.ethz.ch (J.F. Löffler).

https://doi.org/10.1016/j.actamat.2022.117630

In this paper, we report investigations on the structural stability of the BMG-forming alloy $Au_{49}Ag_{5.5}Pd_{2.3}Cu_{26.9}Si_{16.3}$ [28]. During heating from the glassy state, this alloy reveals complex crystallization kinetics in which different phases and metastable structures are involved [29]. However, no data on isothermal structure formation in the glassy state and the stability of this glass exist. To avoid the influence of quenched-in nuclei, we focus here on CHGs by supplying sufficiently fast quenching from the melt. To our best knowledge, the aging kinetics of such a defined metallic glass have not been investigated before in detail.

2. Experimental procedure

2.1. Sample preparation

The elements Au (99.95%), Cu (99.9%), Ag (99.5%), Si (99.95%), and Pd (99.95%) were pre-alloyed via repeated induction melting to a sample with atomic composition $Au_{49}Ag_{5.5}Pd_{2.3}Cu_{26.9}Si_{16.3}$. The alloying was performed in a quartz tube, which was sealed under 99.999% pure Ar atmosphere. The mass loss during this alloying was near the detection limit of laboratory balances, so that the actual composition compares to the nominal composition. The alloy was then processed by melt spinning in 5N+ pure He atmosphere, generating CHG ribbons of approximately 30 μm thickness [17].

2.2. Conventional differential scanning calorimetry

Conventional differential scanning calorimetry (DSC) measurements were performed on samples with a mass of about 30 mg, using a Mettler-Toledo DSC 1 equipped with an FRS 5 sensor and a Huber intracooler TC100. The DSC cell was purged with argon (30 ml min^{-1}), and the transformation temperatures and enthalpies were measured with a heating rate of 10 K min^{-1}. Stochastic temperature modulated DSC (TOPEM) was used to measure the heat capacity [30]. Measurement parameters were the underlying heating rate (here, 1 K min^{-1}), pulse height (±1 K), and pulse width (30 to 35 s). For the evaluation, a calculation window of 300 s was applied. A reference measurement with sapphire using the same modulation parameters was also performed. Well oxidized 40 ml Al crucibles were deployed in all measurements.

2.3. Fast differential scanning calorimetry

FDSC measurements were performed using a Mettler-Toledo Flash DSC 2+ operated with a UFH 1 sensor, described in Ref. [17]. The sample support temperature in the calorimeter was set to −80 °C using a Huber intracooler TC100, and the sensor was purged with argon at a flow rate of 60 ml min^{-1}. The melt-spun ribbons were cut under a stereomicroscope into small pieces with a surface of approximately 10^4 μm^2. Their mass was estimated using the melting enthalpy of $\Delta H_m = 40.4$ J g^{-1} [11] to be between 20 ng and 200 ng. For such samples no size-dependent nucleation and crystallization is expected [10]. For an easier positioning of the sample and to prevent its jumping due to stress release in the glass transition region, the active zone of the sensor (at the sample side) was wetted with a small amount of silicon oil (AK 60,000 from Wacker) before the first heating cycle.

2.4. Measurement methods for studying nucleation by FDSC

Based on Tammann's approach [31], Schick et al. proposed a two-step method to study nucleation in polymers by FDSC [19,32]. A scheme of the temperature program is given in Fig. 1a. The sample is cooled from the equilibrated melt above the liquidus temperature, T_L, to a temperature at which the nucleation process is studied. The cooling rate in this step must be high enough that neither crystallization nor nucleation occur during cooling. The number of nuclei formed during the annealing treatment (blue line in Fig. 1a) determines the number of crystalline grains that will form in a subsequent crystallization step at higher temperatures (green line). After rapid cooling, the resulting crystalline structure is then analyzed in a subsequent heating segment (red line). It must be emphasized that the measured results of this analysis depend crucially on the heating and cooling rates before and after the crystallization step and the crystallization temperature. The heating rate from the nucleation to the crystallization step must be sufficiently high to prevent further nucleation during heating, but also to allow for a survival of the nuclei that formed during the nucleation step. The crystallization temperature must be chosen in such a way that the crystallization rate is moderate, in order to extract the number of nuclei from that of the crystallites without further nuclei formation. The subsequent cooling rate must be high enough to freeze the semi-crystalline structure, and the final heating rate for microstructure analysis must be sufficiently high to prevent not detectable structural modifications. It is thus obvious that the technique requires extensive studies to find the optimum experimental parameters.

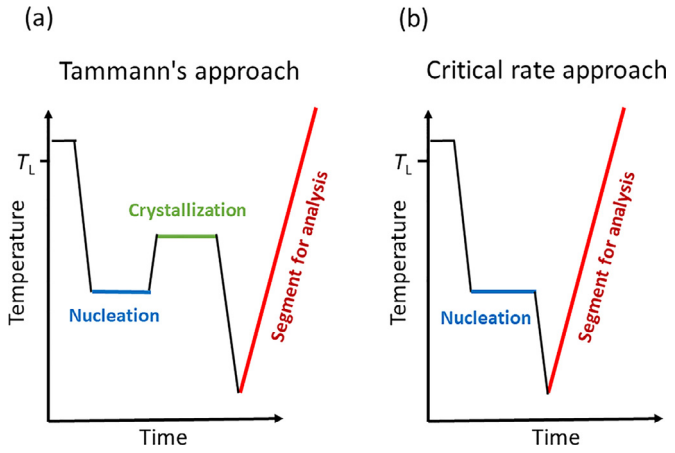

Fig. 1. Different approaches to study nucleation processes by FDSC. (a) Two-step process according to Tammann, and (b) a one-step process using the critical cooling and heating rates of a CHG.

An alternative approach to determine the nucleation kinetics is a method relying on the critical heating and cooling rates of a CHG (Fig. 1b). When cooling the melt with at least the critical cooling rate of a CHG there is no nuclei formation upon cooling, but only during the nucleation step (blue line in Fig. 1b), where the CHG transforms to a SDG, i.e. a glass with nuclei [17]. Upon heating with the critical heating rate of a CHG (red line), crystallization is sensitive to the nuclei that formed during the nucleation step. Thus, using this technique, only two easily to be determined parameters are needed to study nuclei formation. It should be mentioned that it is not necessary to generate a CHG in the first cooling step. If it is not possible to generate a CHG upon cooling, the effect of pre-existing nuclei may be measured without the nucleation step, which then has to be considered in the evaluation of the measurements with nucleation. It is only important that the heating rate in the analysis segment is fast enough to avoid any additional nuclei formation. The critical rate approach has been used in the present study.

3. Results

The critical cooling rate to form a CHG in $Au_{49}Ag_{5.5}Pd_{2.3}Cu_{26.9}Si_{16.3}$ is 4000 K s^{-1}, while it is 500 K s^{-1} to form a SDG.

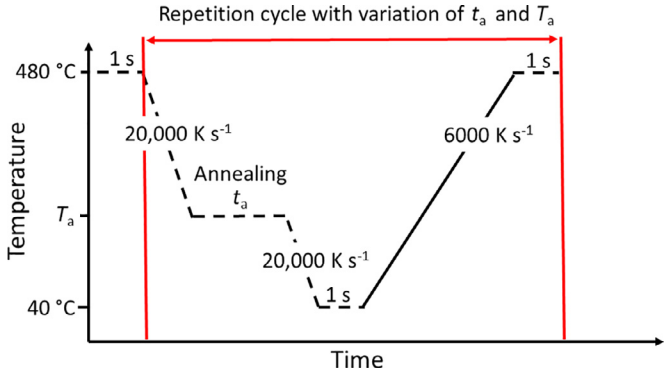

Fig. 2. Schema of the FDSC temperature program to study the behavior of the Au-based glass upon annealing at T_a over times t_a.

The critical heating rate at which no crystallization occurs during heating is 6000 K s^{-1} for a CHG [17]. To generate a CHG during cooling we selected a cooling rate of 20,000 K s^{-1}, which is significantly faster than the critical rate. As heating rate we selected the critical rate of 6000 K s^{-1} to avoid crystallization of the non-nucleated material. Because of the high scanning rates, the measurements were performed on a sample with a mass of 23 ng.

Here we define the glass transition temperature, T_g, as the limiting fictive temperature [33,34]. This is determined via creating the glass upon cooling from the melt with a rate β_c and heating the glass with a rate $\beta_h = |\beta_c|$, and correcting the influence of thermal lag by averaging the glass transitions from the cooling and heating cycles [35]. In this way, the glass transition temperature, T_g, of the CHG cooled at 20,000 K s^{-1} was determined as 174.5 °C.

A schema of the temperature program to measure the behavior during annealing (nucleation step in Fig. 1b) is shown in Fig. 2. The annealing temperature, T_a, was varied between 168 °C and 118 °C in steps of 10 K, and the annealing time, t_a, was varied between 0.01 and 100,000 s. The heating curves were conducted at 6000 K s^{-1}.

Fig. 3 shows for the example of T_a = 138 °C (≈ 35 K below T_g) a set of heating curves after different annealing times. For reference, the heating curves of the non-annealed CHG and of the completely crystallized sample (after cooling at 1 K s^{-1}) are displayed as bold curves. As expected, the curve of the non-annealed CHG shows only the step of the glass transition and no further structural changes during heating. The main effect for the completely crystallized sample is the melting peak above 350 °C. The crystalline material also shows a slight step-like anomaly of the heat capacity at around 250 °C, which is characteristic for the studied alloy.

The first process that occurs during annealing is structural relaxation, as seen in Fig. 3a. The enthalpy relaxation peak increases with increasing annealing time from t_a = 0.01 s and reaches a maximum at $t_a \approx 1$ s. Further annealing does not influence the heat flow curves, and the measurement curves retain their shape for annealing times between 20 s and 100 s.

At further annealing, exothermal crystallization peaks and subsequent endothermal melting peaks appear in the heating curves (Fig. 3b). With increasing t_a the size of the crystallization peak increases and the peak temperature decreases. The size of the final melting peak also increases with increasing annealing time. The area of both peaks is approximately the same for a given annealing time, which indicates that the enthalpies of the exothermal crystallization and endothermal melting events sum up to zero.

Heating curves after annealing between 12,000 s and 18,000 s are shown in Fig. 3c. In these curves the intensity of the glass transition, Δc_p, decreases with increasing annealing time and the crystallization peak reveals a different shape. Additionally, the heat flow after the glass transition slightly increases and eventually evolves into a small endothermal transformation peak at about 240 °C. The subsequent crystallization peak decreases with increasing annealing time. The shape change of the crystallization peak (compared to Fig. 3b) indicates a change in the crystallization kinetics. The final melting peak reveals only little increase in intensity.

Fig. 3d displays the development of the heating curves for $t_a \geq$ 20,000 s. No glass transition appears and the melting peak does not vary. The sample now has completely crystallized during annealing. However, the low-temperature endothermal peak and the following exothermal peak vary with increasing t_a, and both decrease with increasing annealing time. The exothermal peak is finally overlaid with an endothermal bulge at about 270 °C.

To characterize the evolution of the sample structure during annealing, different properties were derived from the heating curves in Fig. 3. These are the intensity of the glass transition, Δc_p, the enthalpy of the structural relaxation, Δh_{relax}, the enthalpy of the primary crystallization, Δh_c, and the temperature of the crystallization peak, T_c. Furthermore, the temperature, T_{m1}, of the endothermal peak at about 240 °C and the temperature, T_{m2}, of the small endothermal event at about 270 °C were evaluated.

The heating curves in Fig. 3a were considered for the evaluation of the enthalpy relaxation, Δh_{relax}. For the determination of Δh_{relax} the measurement curves after annealing at t_a, $\Phi(T,t_a)$, were subtracted by the curve of the non-annealed sample, $\Phi(T,0)$. The resulting peak was then integrated in the temperature interval below (T_{min}) and shortly above the glass transition range (T_{max}) [27,36,37], which results in:

$$\Delta h_{relax}(t_a) = \int_{T_{min}}^{T_{max}} [\Phi(T,t_a) - \Phi(T,0)]dT. \quad (1)$$

Furthermore, the total enthalpy, Δh_{tot}, describes approximately the crystallization process during annealing. This is the sum of the enthalpy of the crystallization peak, Δh_c, and the melting peak, Δh_m, i.e. $\Delta h_{tot} = \Delta h_c + \Delta h_m$. We have to take into account that the exothermal crystallization enthalpy, Δh_c, is negative. If Δh_{tot} has a significant positive value, crystals have formed during annealing (Fig. 3c), while $\Delta h_{tot} \approx 0$ indicates only nuclei formation during the annealing step (Fig. 3b). This approximation neglects the temperature dependence of the transformation enthalpy [38]. However, because of the high heating rate of 6000 K s^{-1}, crystallization occurs at relatively high temperatures and melting at relatively low temperatures (Fig. 3), because in the latter case a metastable solid phase would melt at lower temperature. For these experimental conditions, the change of the crystallization and melting enthalpies with temperature is therefore small and within experimental uncertainty, which results mainly from the base line selection in the evaluation. The practicability in using Δh_{tot} to characterize the crystallinity of metallic alloys by FDSC also results from the proportionality of Δc_p and Δh_{tot} for this alloy [17], where the ratio $\Delta c_p / \Delta c_{p,0}$ is the amount of amorphous fraction ($\Delta c_{p,0}$ is the intensity of the glass transition of a monolithic glass) and $\Delta h_{tot} / \Delta h_{tot,1}$ is the crystallinity ($\Delta h_{tot,1}$ is the enthalpy of the fully crystallized alloy without amorphous components). Thus, a linear relation of the form

$$\frac{\Delta c_p}{\Delta c_{p,0}} = 1 - \frac{\Delta h_{tot}}{\Delta h_{tot,1}} \quad (2)$$

is expected. The corresponding data for semi-crystalline alloys indeed follow Eq. (2) within experimental uncertainty, which is shown in Fig. 4 for the samples annealed at 138 °C and 148 °C.

Eq. (2) is often violated in nearly fully crystallized material where the crystallization temperature is much lower than the melting temperature. In such a case, solid-solid transitions with

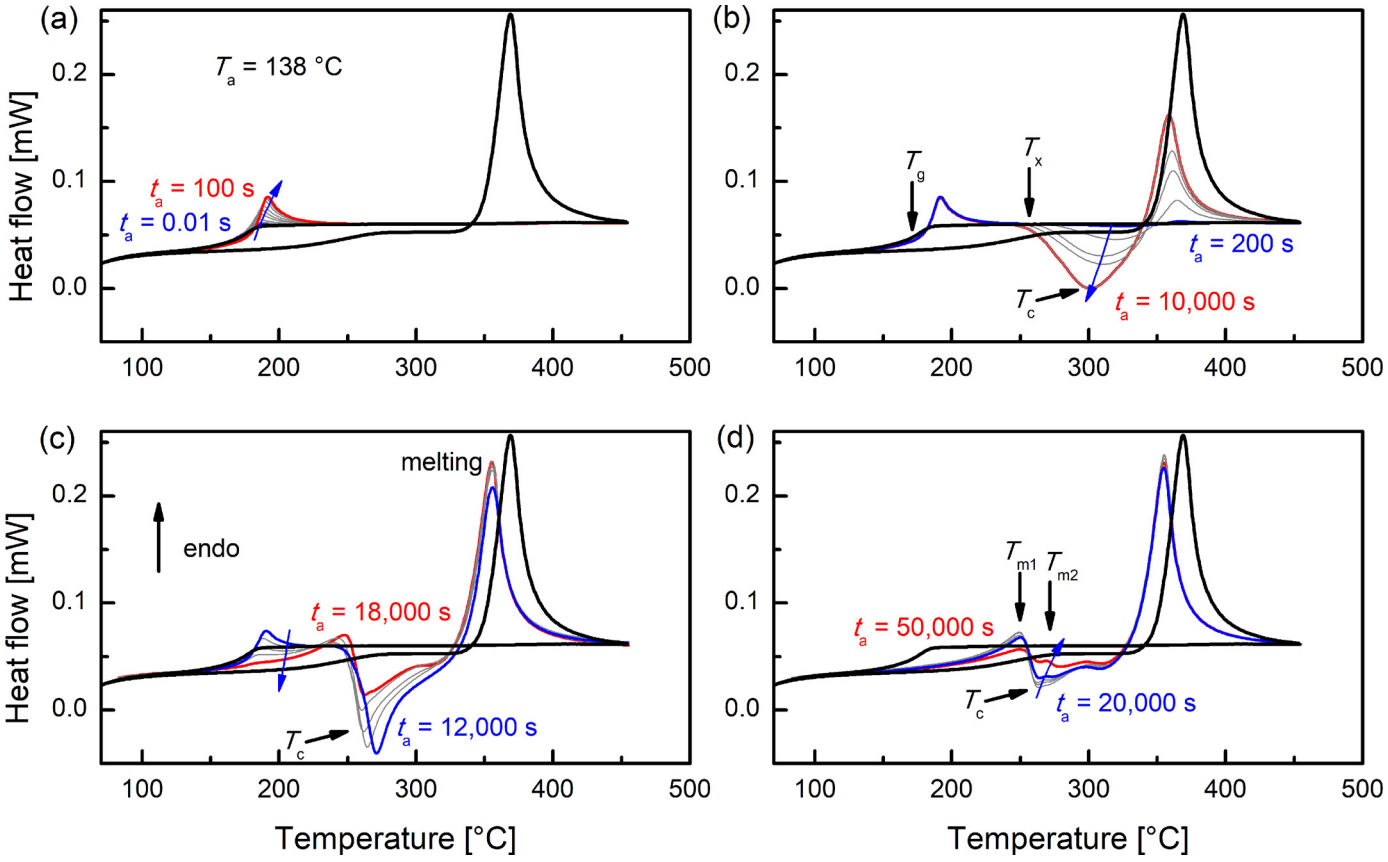

Fig. 3. FDSC heating curves of CHG performed with a rate of $\beta_{h,crit}$ = 6000 K s^{-1} after different annealing times at 138 °C. For comparison the curves of a non-annealed and a slowly cooled (1 K s^{-1}) crystalline sample are added in each diagram and shown in bold. The blue arrows indicate the variation of the curves during annealing. The onset of the primary crystallization is T_x, whereas the crystallization peak is represented by T_c. (a) At annealing times between 0.01 and 100 s the curves reveal enthalpy relaxation. (b) After annealing between 200 and 10,000 s crystallization occurs during heating, resulting from nuclei formation during the annealing step. (c) After annealing between 10,000 and 20,000 s the glass transition intensity reduces, due to crystallization during the annealing step. (d) After annealing for more than 20,000 s, the material is completely crystallized and modifications in the curve are caused by structural perfection, where the structure evolves in the direction of higher thermodynamic stability.

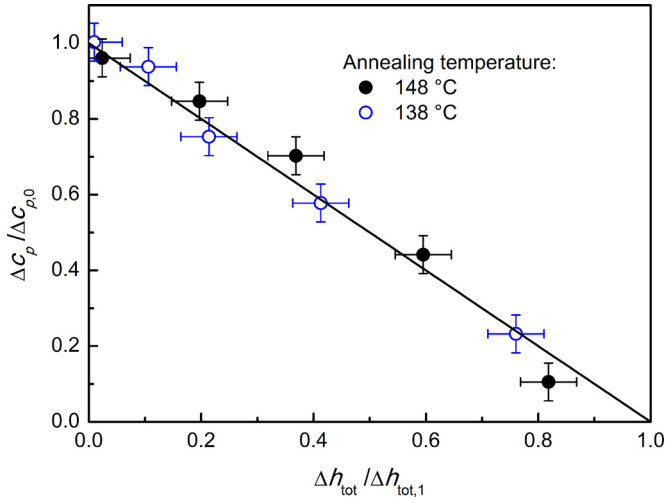

Fig. 4. Amorphousness determined from the intensity of the glass transition versus crystallinity determined by Δh_{tot}. The solid line represents eq. (2).

transformations to more stable modifications are often observed, as presented in Section 4.6.

A known problem for the evaluation of transformation enthalpies from DSC curves is the selection of the baseline for peak integration. The baseline represents the underlying sensible heat flow, which is related to the temperature change of the sample and proportional to the heat capacity, and the baseline-subtracted peak is the latent heat flow component [30,39]. To minimize the relative uncertainty we deployed three different kinds of baseline in dependence of the structural variation during the measurements:

(1) For relatively short annealing times (Fig. 3a,b) the initial sample is a monolithic glass (without or with nuclei). Above the glass transition, the sample becomes a liquid. The extrapolated curve of the non-annealed sample above the glass transition was thus taken as baseline.
(2) For semi-crystalline samples (Fig. 3c) the heat capacity after the glass transition has a value between that of the supercooled liquid and the crystalline sample. In this case, for each t_a an extrapolated line from about 200 °C to the liquid's temperature at the end of the measurement was taken as baseline.
(3) In the case of crystalline samples (Fig. 3d) the baseline was constructed by using the heating curve after slow cooling (1 K s^{-1}). In this measurement curve, the melting peak was substituted by a linear line drawn from the beginning to the end of the melting event, and the resulting curve was taken as baseline.

For the determination of Δh_{tot} all exothermal and endothermal peaks were in between the integration limits. For the evaluation of Δh_c the integration limits were obtained from the intersection points of the measured curve and the baseline.

The intensity of the glass transition, Δc_p, is related to the crystallinity of the sample before heating, α, and the total enthalpy

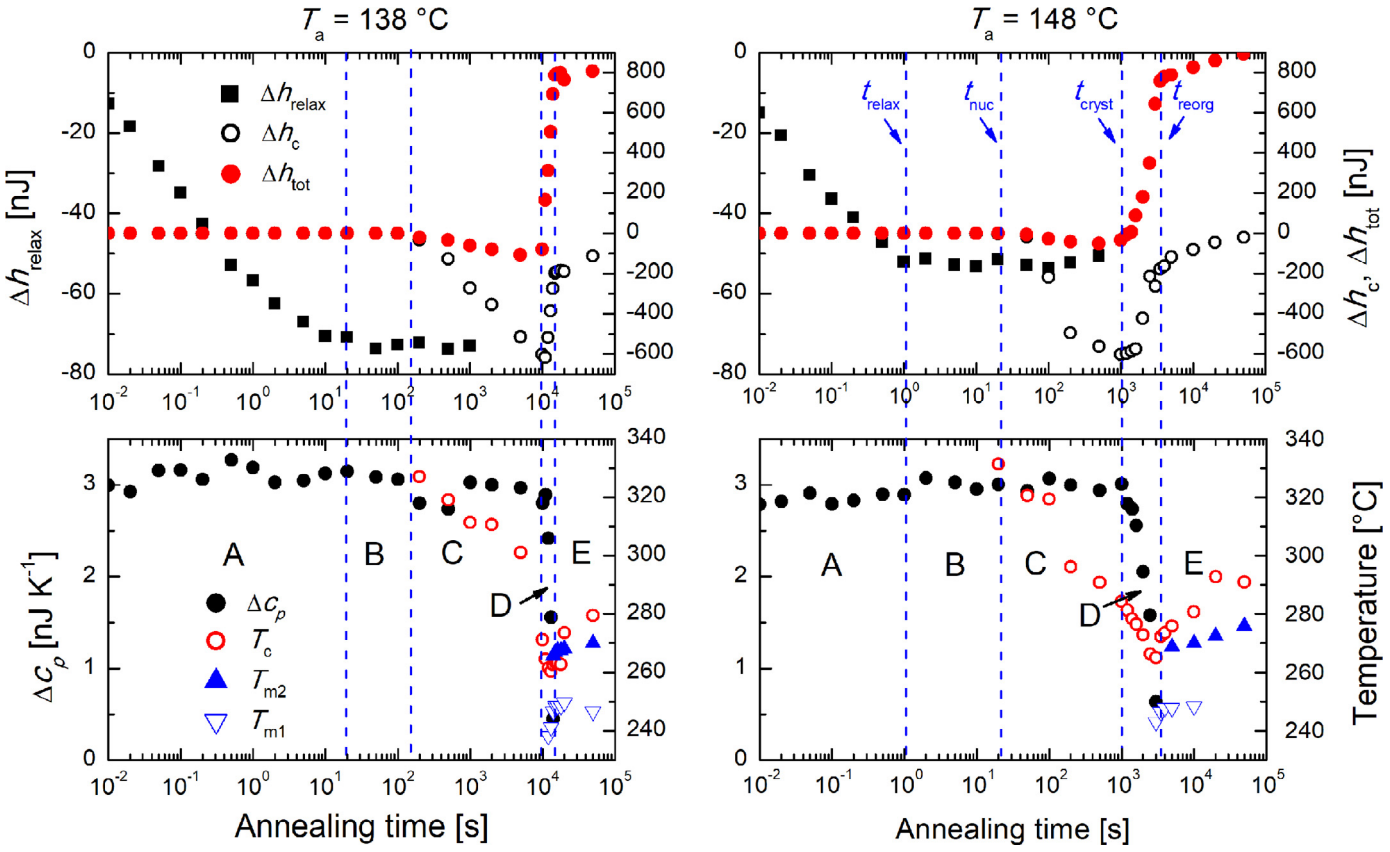

Fig. 5. The change of different properties during annealing (left for T_a = 138 °C and right for T_a = 148 °C). The upper diagrams display the enthalpy relaxation (Δh_{relax}), crystallization enthalpy (Δh_c) and total enthalpy (Δh_{tot}). The lower diagrams display the intensity of the glass transition (Δc_p), peak temperature of crystallization (T_c), and minor melting peaks (T_{m1} and T_{m2}).

Δh_{tot}, according to [17]:

$$\alpha \propto \left(\Delta c_{p,0} - \Delta c_p\right) \propto \Delta h_{tot}. \quad (3)$$

In Fig. 5, the evaluated properties of differently annealed glasses are plotted as a function of t_a for annealing temperatures of 138 °C and 148 °C. The vertical lines separate different phases of the annealing process. The line at the end of section A represents the time, t_{relax}, at which structural relaxation is finished and Δh_{relax} reaches a maximum negative value. At the end of section B (at t_{nuc}) a crystallization peak appears in the heating curve. In section C the crystallization enthalpy, Δh_c, increases towards negative values and reaches finally a maximum exothermal enthalpy of about −600 nJ (for both temperatures). The limits of section D are the onset time of crystallization, t_{cryst}, and the onset time of the process for structural perfection, t_{reorg}. Structural perfection means here the evolution of the structure towards higher thermodynamic stability, e.g. by lowering the defect density, increasing the crystal size, or via a transformation towards a more stable crystalline modification. In this time range, the intensity of the glass transition decreases due to crystallization during annealing. In the last section E, the fully crystalline material changes its structure, which is reflected in the variation of the low-temperature endothermal peaks at T_{m1} and T_{m2}.

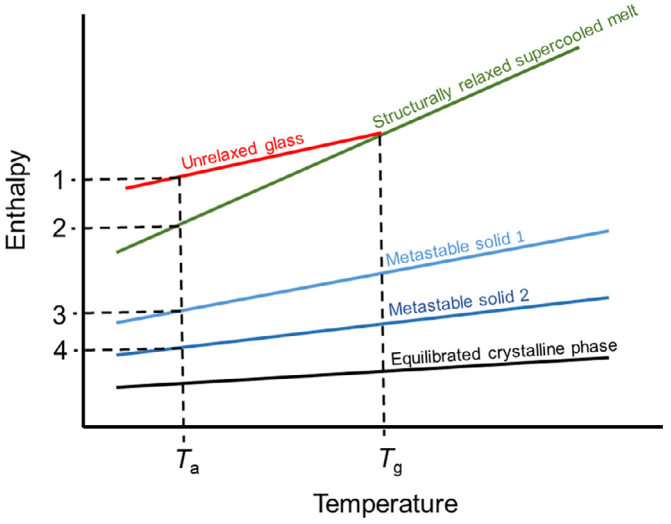

Fig. 6. Schematic enthalpy-temperature diagram, illustrating the evolution of various phases near the glass transition, T_g. During annealing of the CHG at T_a the enthalpy reduces from position 1 to 4.

4. Discussion

4.1. Different processes during annealing

Fig. 6 plots for various possible phases the enthalpy curves as a function of temperature far below the equilibrium melting temperature around the glass transition temperature, T_g. The equilibrated crystalline structure is the most stable polymorph and reveals the lowest enthalpy. Above T_g, the supercooled melt is the least stable and has the highest enthalpy. In the glass transition range, the supercooled melt vitrifies upon cooling and the slope of the enthalpy curve is reduced towards that of the stable crystalline structure. Two metastable polymorphic modifications are added in between, referred to as metastable solids 1 and 2. The metastable modifica-

tion 1 is less stable than modification 2. These metastable modifications are usually not single crystalline phases or intermetallic compounds, but non-equilibrated crystalline structures such as nano-compounds of different phases with a high contribution of interface energy or non-equilibrated supersaturated solid solutions. This is especially the case for structures that form at low temperatures due to a reduced atomic mobility. These metastable solid modifications can be very complex in the case of Au-based BMG-forming alloys [40].

The concept of Fig. 6 is discussed in detail in Refs. [17,38]. Furthermore, Ivanov et al. [29] indeed recently identified via in-situ TEM different metastable phases that formed above the glass transition in $Au_{49}Ag_{5.5}Pd_{2.3}Cu_{26.9}Si_{16.3}$.

To describe the different processes that occur during annealing of the CHG at T_a we use the schematic enthalpy-temperature diagram of Fig. 6. Examples of the related heat flow curves measured during heating after annealing are plotted in Fig. 3.

Rapid cooling of the melt results in an unrelaxed glass of highest enthalpy (position 1). Upon annealing at T_a, structural relaxation occurs first (section A in Fig. 5). The enthalpy of the glass decreases and tends towards the enthalpy of the structurally relaxed supercooled melt (position 2). In Fig. 5 this period of annealing is characterized by an increase of the exothermal relaxation enthalpy, Δh_{relax}, (towards negative values) and the invariance of all other evaluated properties.

In section B, all properties are constant and the enthalpy of the glass remains at position 2. This is the incubation time for nucleation, which is finished at t_{nuc}. The latter denotes the time where an onset of nucleation can be detected.

Also in section C the sample remains at position 2 and nuclei form during annealing. This process is indicated by the appearance of a crystallization peak in the heating curve (Fig. 3b). The exothermal crystallization enthalpy, Δh_c, increases (towards more negative values) and T_c decreases with increasing t_a (Fig. 5). All other properties are still invariant during nucleation. The end of this section is characterized by a maximum exothermal crystallization enthalpy at t_{cryst}. Up to this time the total transformation enthalpy, Δh_{tot}, remains at zero, indicating that the sample is completely amorphous up to t_{cryst}.

Crystallization then occurs in the relatively narrow time window between t_{cryst} and t_{reorg} (section D). This is indicated in Fig. 5 by a decrease of Δc_p and the endothermal increase of the total enthalpy. The exothermal crystallization enthalpy, Δh_c, decreases with increasing t_a because the sample already crystallizes during t_a and thus less during subsequent heating. A similar scenario was reported for a Ce-based BMG-forming alloy [24] and selenium [25] during annealing in the glassy state, but the incubation period was not analyzed for that material. In section D the temperature of the crystallization peak, T_c, further decreases because the initial crystals that form in the sample upon annealing accelerate crystallization during the subsequent heating. At $t_a = t_{reorg}$, the sample is completely crystallized and no glass transition appears in the heating curve. In this segment a low-temperature transformation peak at T_{m1} appears. The sample transforms during this crystallization to a metastable crystalline phase 1 and reduces its enthalpy from position 2 to position 3, as illustrated in Fig. 6.

At the beginning of the last segment E, the sample is completely crystalline and all measured effects are related to changes in the metastable crystalline structure. During this annealing period, the crystalline structure that formed during annealing at $t_a < t_{reorg}$ transforms towards a more stable modification. We term this time segment as “period of structural perfection”. In Fig. 6, this is the enthalpic transformation from position 3 to 4. The heating curves in Fig. 3d show that in section E the crystallization peak decreases and T_c increases with progressing annealing time. Additionally, the low-temperature melting peak at T_{m1} decreases and finally disappears, whereas a new peak at T_{m2} emerges.

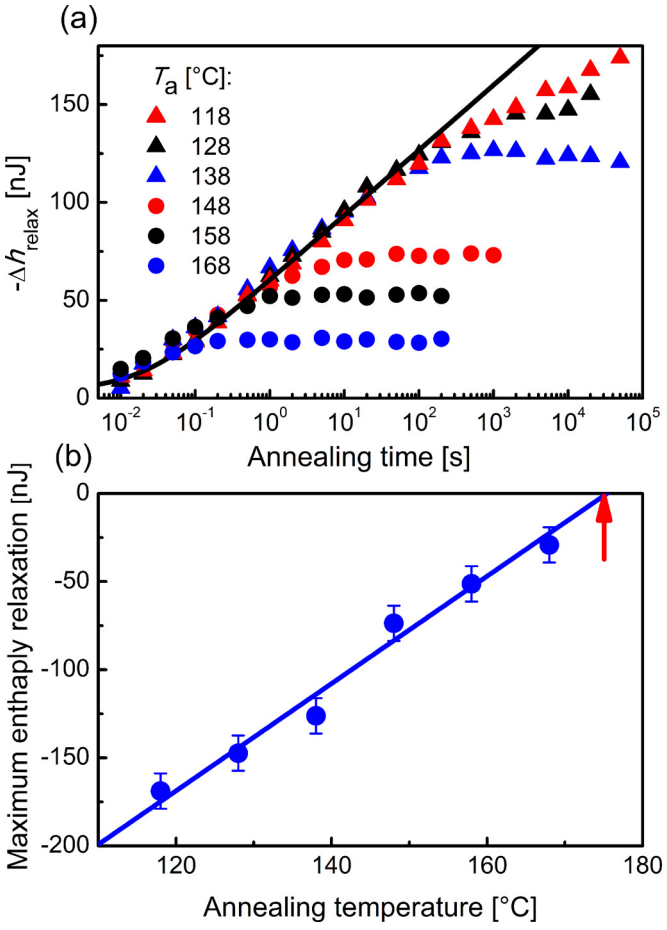

Fig. 7. (a) Structural enthalpy relaxation as a function of annealing time for different annealing temperatures. The black curve is a guide for the eyes. (b) Maximum enthalpy relaxation as a function of annealing temperature and linear fit to the data (blue line). The red arrow indicates the glass transition temperature of the non-annealed CHG after cooling at a rate of 20,000 K s^{-1} (174.5 °C).

In the following, the different stages that occur during annealing are discussed in more detail.

4.2. Structural relaxation in the vitrified state

Fig. 7a shows the enthalpy of structural recovery, $\Delta h_{relax}(T_a, t_a)$, as a function of annealing time for different annealing temperatures. The time dependence of the structural relaxation is usually described by a stretched exponential Kohlrausch function [41]:

$$\Delta h_{relax}(T_a, t_a) = \Delta h_{relax,m}(T_a)\left(1 - \exp\left(-\left(\frac{t_a}{\tau_K(T_a)}\right)^{b(T_a)}\right)\right), \quad (4)$$

where $\Delta h_{relax,m}$ is the maximum change of the enthalpy during structural relaxation, τ_K is the Kohlrausch time constant, and $0 < b \leq 1$ is the related exponent. All of these parameters depend on the annealing temperature T_a.

The maximum enthalpy during isothermal structural relaxation is

$$\Delta h_{relax,m} = \int_{T_L}^{T_a} \left[c_{p,\beta c}(T) - c_{p,L}(T)\right] dT, \quad (5)$$

where $c_{p,\beta c}(T)$ is the heat capacity curve during cooling of the melt from the liquidus temperature, T_L, to the annealing temperature,

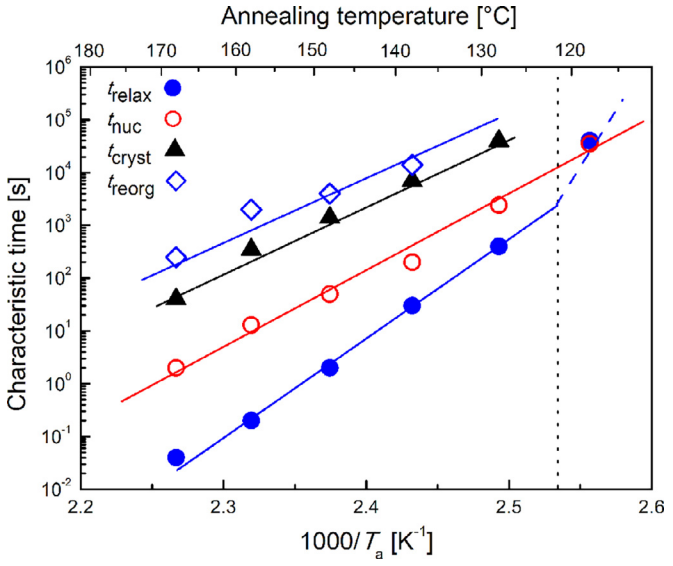

Fig. 8. Characteristic times of different processes as a function of reciprocal annealing temperature: (i) time for complete structural relaxation of the glass (t_{relax}), (ii) incubation time for nucleation (t_{nuc}), (iii) onset time for crystallization (t_{cryst}), and (iv) time after which the initially formed crystals reorganize (t_{reorg}). The lines are guides for the eye.

T_a, with a cooling rate β_c. The (extrapolated) heat capacity of the supercooled liquid is $c_{p,L}(T)$.

The temperature and annealing-time dependent relaxation enthalpy follows first a temperature-independent universal relaxation curve (Fig. 7a) before Δh_{relax} approaches the temperature-dependent maximum value of the enthalpy relaxation, $\Delta h_{relax,m}$. Such a behavior is typical for the structural relaxation of glasses [13].

The end of the structural relaxation process, t_{relax}, is defined as the time at which the relaxation enthalpy reaches its maximum, $\Delta h_{relax,m}$. In Fig. 7b, $\Delta h_{relax,m}$ is plotted as a function of annealing temperature. For the lowest T_a (118 °C) the glass could not completely relax within the time frame of the experiment (Fig. 7a). For this relative low temperature (ca. 110 K below T_g), the curve indicates an additional relaxation process that starts at $t_a \approx 1000$ s. Such a low-temperature relaxation process at around 100 °C was also reported for a Au-based glass in temperature-modulated DSC measurements [42], and a second relaxation process at low temperature was also recently seen in amorphous selenium [25]. Such behavior may point to fundamental changes in the atomic dynamics, as suggested by a transformation of the glass-forming liquid from fragile to strong [43,44] or a change of the low-temperature relaxation kinetics in the glass [25,45-47]. For $Au_{49}Ag_{5.5}Pd_{2.3}Cu_{26.9}Si_{16}$, Monnier at al [48] recently reported a decoupling of vitrification and α-relaxation in the temperature range where we observe a splitting of the relaxation processes.

The limiting fictive temperature can be determined by an extrapolation of $\Delta h_{relax,m}(T_a)$ to zero (Fig. 7b), which presents the T_g of the non-relaxed glass as 175 °C. This value agrees well with the direct determination of T_g = 174.5 °C (see above) and illustrates the self-consistency of the methods.

The annealing time, t_{relax}, to reach the structurally equilibrated melt is plotted as a function of the reciprocal temperature in an Arrhenius presentation in Fig. 8 (blue circles). Arrhenius-like behavior is seen down to T_a = 128 °C (≈ 45 K below T_g), while for T_a = 118 °C, t_{relax} is significantly larger than expected from an extrapolation of the high-temperature data. The significant slowdown of the structural relaxation at low temperatures indicates differences in the atomic dynamics of the glass, what is not expected within the framework of a classical, phenomenological description of the glass transition.

4.3. Nucleation

Nucleation is measured in the time period where enthalpy relaxation is complete but no crystalline structure has yet formed (i.e. Δc_p is the same as for the non-annealed CHG). Because the heating rate applied corresponds to the critical heating rate of the CHG, nuclei do not form during heating. The crystallization peak observed during heating (Fig. 3b) must therefore result from nucleation during the isothermal annealing step (see also Fig. 1b).

The incubation time for nucleation during annealing, t_{nuc}, relates to the onset of $\Delta h_c(t_a)$ in Fig. 5. This incubation time is also plotted in Fig. 8. For $T_a > 120$ °C, t_{nuc} is much larger than the time for complete structural relaxation, t_{relax}.

Perepezko and Hildal defined the onset time for nucleation as the time when a nucleation event occurs in the respective volume. Accordingly, it follows [49]

$$\log t_{nuc} = A_1 + \log \eta - \log T + \frac{A_2}{T\ G_v^2}, \tag{6}$$

where A_1 is the pre-exponential factor, the constant A_2 characterizes the surface-tension contribution for nucleation, η is the temperature-dependent melt viscosity and G_v is the Gibbs free energy difference between liquid and crystalline phase. In a first approximation, $G_v(T)$ can be expressed by the Tammann-Meissner-Rie (TMR) equation [50]

$$G_v(T) = \frac{\Delta h_f}{T_L}(T_L - T), \tag{7}$$

where T_L is the liquidus temperature and Δh_f is the enthalpy of fusion. If we assume an approximate Arrhenius behavior for the temperature dependence of the viscosity, the validity of the Maxwell equation, and a constant ratio between the shear-stress relaxation time and the thermal retardation time, τ_s, it follows the approximation [51]

$$\log \eta(T) = A + \log \tau_s(T) \approx A_0 + \frac{E_a}{2.3\ R\ T}, \tag{8}$$

where E_a is the apparent activation energy of relaxation during the glass transition, R is the gas constant, and A and A_0 are constants.

In the temperature range of consideration, log$T$ can be assumed to be constant. By inserting Eqs. (7) and (8) into (6), it then follows

$$\log t_{nuc} = B_1 + \frac{E_a}{2.3\ R\ T} + \frac{B_2}{T(T_L - T)^2} \tag{9}$$

with the constants B_1 and B_2. The liquidus temperature of the Au-based glass is T_L = 644 K [28]. Because the measured nucleation occurs more than 200 K below T_L, we expect diffusion-controlled nucleation. Thus, eq. (9) can be simplified to:

$$\log t_{nuc} = B_0 + \frac{E_a}{2.3\ R\ T}. \tag{10}$$

A comparison of the curves of t_{nuc} and t_{relax} in Fig. 8 shows that the slope and thus the activation barrier for nucleation (274 kJ mol^{-1}) is much lower than that for structural relaxation (374 kJ mol^{-1}). Extrapolation of the activation curves indicates a crossover of structural relaxation and nucleation at about 106 °C. We measure, however, a slow-down of the structural relaxation below 120 °C, which shifts the crossover of the $t_{relax}(T)$ and $t_{nuc}(T)$ curves to higher temperatures. In fact, t_{relax} and t_{nuc} coincide at T_a = 118 °C. At temperatures lower than T_a = 118 °C it is thus expected that nucleation occurs before structural relaxation is completed. This expectation agrees well with results on various low-molecular-weight organic and inorganic materials where nucleation and crystallization set in at low temperature before the glass completely relaxes structurally [26,52-54].

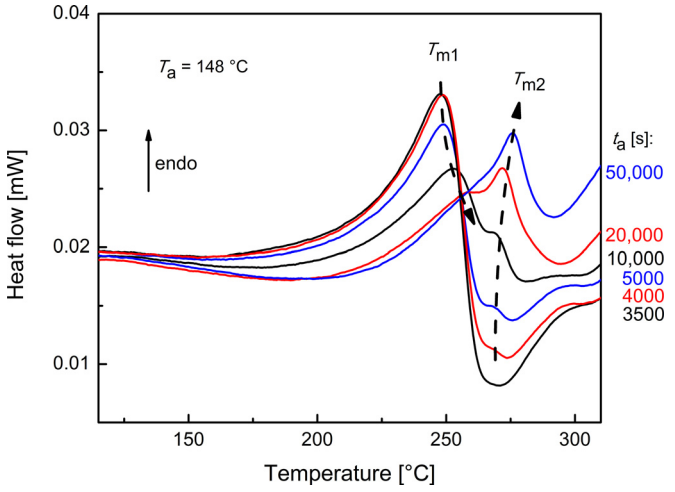

Fig. 9. Heat flow curves showing the development of the low-temperature melting peaks at T_{m1} and T_{m2} during annealing of the Au-based CHG at 148 °C.

Via annealing in the time period between t_{nuc} and t_{cryst}, clusters form that can act as nuclei during heating. After reaching t_{nuc}, the crystallization peak, T_c, in the heating curve decreases and the exothermal crystallization enthalpy, Δh_c, increases (towards more negative values) with increasing annealing time (Fig. 5), while the intensity of the glass transition, Δc_p, and the total enthalpy ($\Delta h_{tot} = \Delta h_c + \Delta h_m \approx 0$) remain constant. Although the embryonic clusters that formed during annealing become less stable during heating, several of them may still be able to grow to a nucleus and initiate crystallization during heating.

4.4. Crystallization

Crystallization can be clearly identified by a decrease of the glass transition intensity, Δc_p, and the simultaneous appearance of a melting peak (Fig. 3c). The low temperature of the melting peak (at about 250 °C) is a clear indication for the low thermodynamic stability of the formed crystalline structure.

For $t_a = t_{cryst}$ the exothermal crystallization enthalpy reaches a maximum of about −600 nJ and decreases towards less negative values with increasing annealing time. This is connected with a decrease in Δc_p and an increase in the endothermal total enthalpy, Δh_{tot}, due to crystallization during annealing (Fig. 5). The crystals that formed during annealing influence the crystallization kinetics during heating. This is indicated by the increase and shape change of the crystallization peak (see Fig. 3c). Crystallization during annealing is finally completed when Δc_p reaches zero.

During crystallization a low-temperature endothermal peak with a maximum at $T_{m1} \approx 240$ °C develops (see Fig. 3c). This is due to the formation of a metastable crystalline phase 1, as indicated in Fig. 6, and agrees with the early finding in various BMG-forming alloys where different crystalline structures form during crystallization below and above the glass transition [55–58].

4.5. Structural perfection

For $t_a \geq t_{reorg}$ the sample is completely crystallized, but the crystals formed during annealing can change their structure within this time period. This is indicated by the development of transformation peaks at T_{m1} and T_{m2} in the subsequent heating curves. For the example of $T_a = 148$ °C, Fig. 9 shows the heat flow curves in the interesting temperature range. After annealing for 3500 s the peak at $T_{m1} = 248$ °C is fully developed and is directly followed by an exothermal crystallization peak. This is the typical heat flow signature for a monotropic solid-liquid-solid transformation during heating [59]. It is remarkable that this melting temperature is in the range of the primary crystallization of non-annealed samples (see Fig. 3 and Ref. [29,42]), which indicates the low stability of the modification formed during annealing. Due to the low atomic mobility at T_a and the expected high nuclei density, it is likely that this modification is nanostructured. This modification appears to be the least stable crystalline structure in $Au_{49}Ag_{5.5}Pd_{2.3}Cu_{26.9}Si_{16.3}$.

After annealing for 4000 s a small endothermal peak appears at $T_{m2} \approx 270$ °C and increases with increasing annealing time. Simultaneously, the peak intensity at T_{m1} decreases and the peak temperature increases slightly. Finally, the peak at T_{m1} disappears and is completely replaced by the transformation at T_{m2}. The maximum temperature of T_{m2} is 275.4 °C. This behavior is an expected consequence of structural perfection resulting from a reorganization during long-time annealing.

The onset time of reorganization, t_{reorg}, is defined as the first-time appearance of the melting peak at T_{m2}. In the activation diagram (Fig. 8) the line of t_{reorg} has a slope similar to the crystallization process during annealing, indicating similar activation energies for crystallization and reorganization.

4.6. Thermodynamic properties

4.6.1. Melting temperature and enthalpy of the metastable modification x1

Ivanov at al. [29] investigated via DSC and FDSC the formation of different solid modifications upon heating a $Au_{49}Ag_{5.5}Pd_{2.3}Cu_{26.9}Si_{16.3}$ glass at a rate between 0.083 and 2000 K s^{-1}. The least stable crystalline modification, x1, that formed at these conditions via primary crystallization at T_{x1} is a nanocrystalline $(Au,Cu)_7Si$ single phase supersaturated in silicon [29].

We compare this modification with the crystalline modifications of the present study, which formed during annealing below the initial glass transition temperature and melted at T_{m1} and T_{m2}, respectively. Via conventional DSC at a heating rate of 10 K min^{-1} we measured for the modification x1 a crystallization temperature of $T_{x1} = 180.0$ °C and a crystallization enthalpy of $\Delta h_{x1} = -2.15$ kJ mol^{-1}. Furthermore, the most stable crystalline modification revealed a melting temperature of $T_m = 350.9$ °C and a melting enthalpy of $\Delta h_m = 5.10$ kJ mol^{-1}. The melting temperature and enthalpy of the modification x1 were further determined by FDSC using a sample of 184 ng in mass. The x1 modification was prepared by heating the sample to the end of the primary crystallization peak at 243 °C with a rate of 100 K s^{-1} (see insert of Fig. 10a). The sample was then cooled with a rate of 20,000 K s^{-1} to 0 °C and heated to 490 °C at rates between 500 and 10,000 K s^{-1}. The FDSC heating curves are shown in Fig. 10a, where the arrows indicate the x1 transformation peak, which shifts to higher temperature with increasing heating rate. At 10,000 K s^{-1} no solid-solid transformation occurs anymore and the remaining endothermal peak originates from the melting of x1. In this way a melting enthalpy of $\Delta h_{m,x1} = 3.185$ kJ mol^{-1} and an onset of melting of 343 °C at this heating rate can be measured.

To determine the correct melting temperature, the thermal lag needs to be considered, which should be measured for the same sample to minimize experimental errors. Here, the most stable solid modification should be used to avoid structural changes during heating. Such structure was prepared by heating the sample to 342 °C (shortly before melting) at a rate of 2 K s^{-1} and subsequent cooling. The sample was then heated at rates, β_h, between 500 and 10,000 K s^{-1} and the onset of the melting peak, T_{on}, was evaluated (Fig. 10b). The figure shows a non-linear dependence of the onset temperature on heating rate. Such a behavior is typical

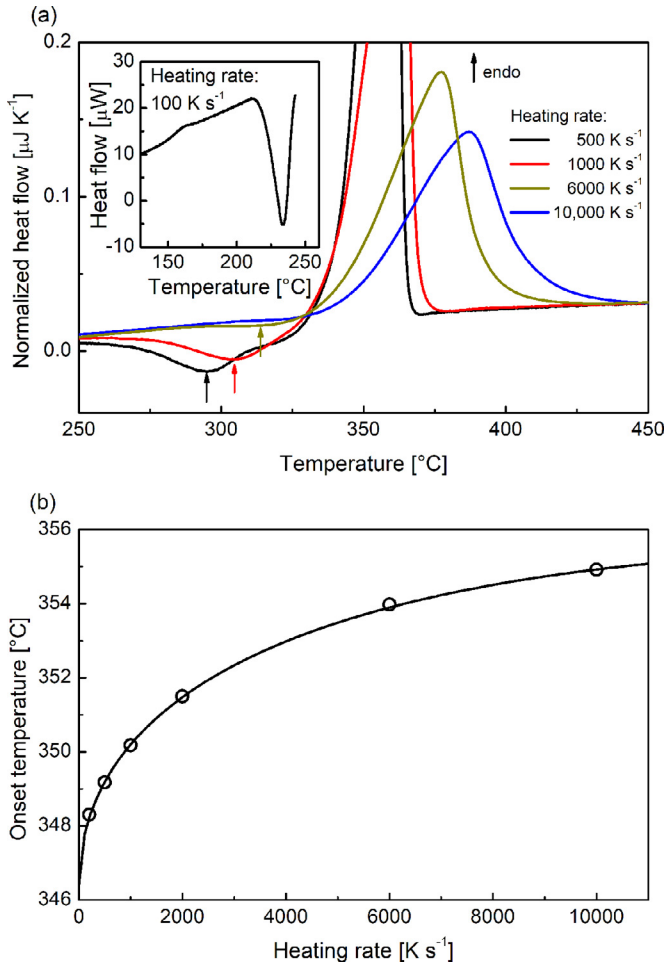

Fig. 10. Determination of the melting temperature for the solid modification x1 formed during heating. (a) The inset shows the FDSC curve for the preparation of the x1 modification by heating the sample to 243 °C with a rate of 100 K s^{-1}. The main diagram shows the melting curves measured at different heating rates after cooling the sample to 0 °C at a rate of 20,000 K s^{-1}. The heat flow is normalized by the heating rate. The arrows indicate the exothermal x1 transformation peaks, which occur up to a heating rate of 6000 K s^{-1}. (b) Heating rate dependence of the onset of melting for the most stable solid modification.

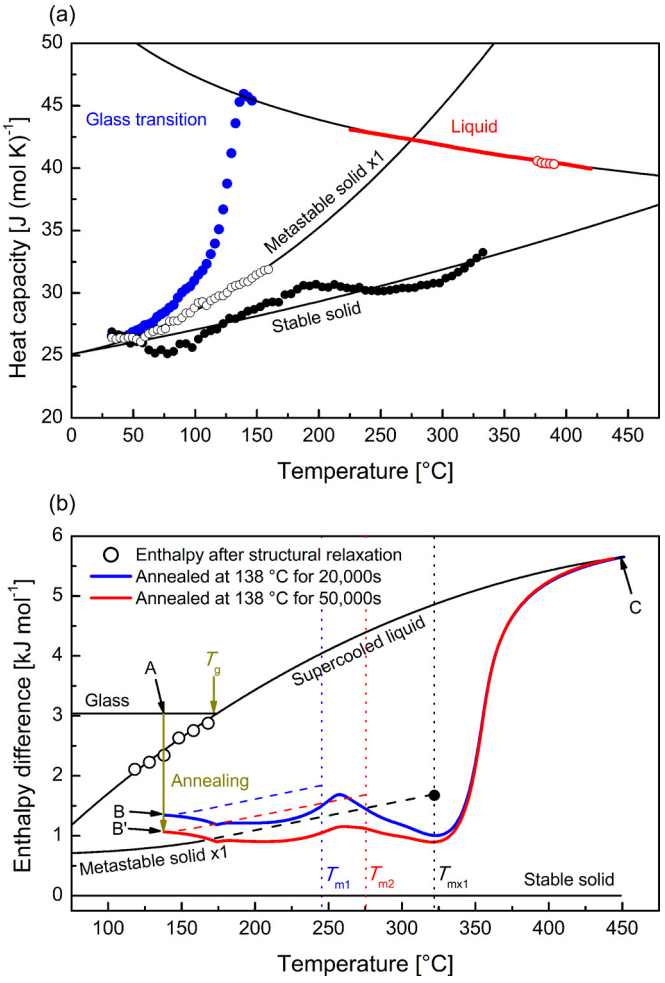

Fig. 11. Heat capacity and enthalpy curves. (a) Heat capacities measured via temperature-modulated DSC (circles) and FDSC (red curve). The heat capacities are fitted using eqs. (12) and (13) (black curves). (b) Enthalpy differences with respect to the most stable solid state (ground state). The solid black circle represents the melting of the modification x1. The open circles indicate the enthalpy at the end of the structural relaxation. The blue and red curves are calculated from the FDSC curves measured after different annealing times at 138 °C to determine the transformation enthalpies at this temperature. The dashed curves are estimated enthalpy curves for the corresponding metastable solid modifications.

for high heating rates [60] and can be described by

$$T_{on} = T_0 + a\,\beta_h + b\,\beta_h^{0.5}, \quad (11)$$

where T_0 is the melting temperature at zero heating rate and a and b are constants. The curve in Fig. 10b is the fitting result. By applying the correction of Eq. (11), a melting temperature of T_{mx1} = 322.1 °C has been determined for the x1 modification.

4.6.2. Heat capacities and reference enthalpies

In a next step, the heat capacities of x1, of the glass, and (for reference) of the most stable crystalline modification and the liquid are determined. The latter data are reported by Dalla Fontana et al. [61] and Louzguine-Luzgin et al. [42]. Due to the significant difference of the data in the literature, we measured the heat capacity using stochastic temperature-modulated DSC (TOPEM). The results are shown as circular dots in Fig. 11a.

To determine the heat capacity in the glassy state (blue circles in Fig. 11a), we first measured an untreated ribbon by TOPEM at temperatures between 30 °C and 400 °C. The sample was then cooled at a rate of 1 K min^{-1} to obtain a sample with the most stable crystalline modification, which constitutes five phases [62]. The heat capacities of this modification (black solid circles in Fig. 11a) and of the liquid (red open circles in Fig. 11a) were subsequently measured.

The least stable solid modification forms upon heating via primary crystallization at T_{x1}. As mentioned, according to Ref. [29] this modification is a nanocrystalline $(Au,Cu)_7Si$ single phase supersaturated in silicon. To prepare this sample state, we heated a ribbon in DSC with a rate of 10 K min^{-1} to 185 °C, which is the end of the primary crystallization peak at this low heating rate. (Note that in the previous FDSC measurements at a heating rate of 100 K s^{-1}, the end of the primary crystallization extended to 243 °C). After rapid cooling the sample to RT by placing it onto a cold metal plate, the heat capacity was measured using TOPEM at a rate of 1 K min^{-1} up to the first indication of a solid-solid transformation at 161 °C (open black circles in Fig. 11a).

To expand the measurement range of the supercooled liquid, the FDSC cooling curves at a rate of 20,000 K s^{-1} were additionally used (red curve in Fig. 11a). The procedure for obtaining heat capacity data from FDSC curves is described in Ref. [38].

At temperatures sufficiently above the Debye temperature, the heat capacity is frequently approximated by polynomials [42,63,64]

such as

$$c_{p,\mathrm{L}} = a_\mathrm{L} + b_\mathrm{L}\,T + c_\mathrm{L}\,T^{-2} \quad (12)$$

for the liquid and

$$c_{p,\mathrm{x}} = a_\mathrm{x} + b_\mathrm{x}\,T + c_\mathrm{x}\,T^{2} \quad (13)$$

for the solid phases. The related fitting curves are the black lines in Fig. 11a. These approximations are used together with the derived transformation enthalpy of the primary crystallization $\Delta h_{\mathrm{x1}} = -2.15$ kJ mol^{-1}, the enthalpy of melting $\Delta h_\mathrm{m} = 5.10$ kJ mol^{-1}, the transformation temperature $T_{\mathrm{x1}} = 180.0$ °C and the melting temperature $T_\mathrm{m} = 350.9$ °C to calculate the curves of the relative enthalpies for the related modifications.

For the most stable solid modification we obtain for the reference temperature $T_0 < T_\mathrm{g}$:

$$\Delta h_\mathrm{s}(T) = \int_{T_0}^{T} c_{p,\mathrm{s}}\,\mathrm{d}T'. \quad (14)$$

For the liquid and the metastable modification x1 we obtain

$$\Delta h_\mathrm{L}(T) = \int_{T_\mathrm{m}}^{T\geq T_0} c_{p,\mathrm{L}}\,\mathrm{d}T' + \Delta h_\mathrm{m} \quad (15)$$

and

$$\Delta h_{\mathrm{x1}}(T) = \int_{T_{\mathrm{x1}}}^{T} c_{p,\mathrm{x1}}\,\mathrm{d}T' + \Delta h_{\mathrm{x1}}. \quad (16)$$

The limiting fictive temperature [33,34] is used to define the glass transition temperature $T_\mathrm{g} = 174.5$ °C. Within experimental uncertainty, we did not find a deviation between the heat capacity of the glass at low temperature and the most stable solid state. Thus, we assume for the relative enthalpy of the glass that

$$\Delta h_{\mathrm{glass}}(T) = \int_{T_\mathrm{g}}^{T\leq T_\mathrm{g}} \frac{\mathrm{d}\Delta h_\mathrm{s}}{\mathrm{d}T'}\,\mathrm{d}T' + \Delta h_\mathrm{L}(T_\mathrm{g}), \quad (17)$$

where $\Delta h_\mathrm{s}(T)$ is the ground state of the stable solid. The enthalpy curves from which the ground state was subtracted are plotted in Fig. 11b (black curves).

The melting enthalpy change between the supercooled liquid and the modification x1 ($\Delta h_{\mathrm{m,x1}} = 3.185$ kJ mol^{-1}, see above) is plotted as a solid black circle in Fig. 11b. This measurement point is far lower than what one would obtain from the extrapolated curve using eq. (16). This illustrates the problem of extrapolating heat capacity data with a quadratic equation (see eq. (13)). Instead, we use here a linear extrapolation by drawing the enthalpy curve $\Delta h_{\mathrm{x1}}(T)$ from the last measured enthalpy value at 161 °C to the explicitly measured melting enthalpy at T_{mx1} (black dashed line in Fig. 11b).

4.6.3. Thermodynamic properties of the crystalline modifications formed during annealing

The maximum enthalpy change (Fig. 7b) was calculated in kJ mol^{-1} (using the corresponding mass and density of the sample) and subtracted from the enthalpy of the glassy state. These data are plotted in Fig. 11b as open black circles, fitting well the data of the equilibrated supercooled liquid. The sample remains in this enthalpy state until crystallization starts.

The relative stability of a crystalline modification formed during crystallization upon isothermal annealing below the initial glass transition T_g can be assessed by determining the maximum enthalpy change. However, the enthalpy change of such slow processes cannot be measured directly. Instead, we use here the law of energy conservation, where the enthalpy change between A and B, Δh(A,B), is equal to the difference of the enthalpy changes of A and B with respect to an equilibrium state C and independent on the pathway: Δh(A,B) = Δh(C,B) - Δh(C,A). The points A, B, and C are indicated in Fig. 11b. The enthalpies are determined by an integration of the heat flow. To compensate for the influence of thermal losses, a measured reference curve is required. For this, we used the heating curve of the completely amorphous sample, $\Phi_{\mathrm{am}}(T)$. In the following we determined the enthalpy curve after annealing for 20,000 s at $T_\mathrm{a} = 138$ °C, $\Phi_{\mathrm{20k}}(T)$, using

$$\Delta h_{\mathrm{20k}}(T) = \int_{T_\mathrm{C}}^{T_\mathrm{a}\geq T\geq T_\mathrm{C}} \left(\Phi_{\mathrm{20k}}\left(T'\right) - \Phi_{\mathrm{am}}\left(T'\right)\right)\,\mathrm{d}T' + \Delta h_\mathrm{L}(T_\mathrm{C}), \quad (18)$$

where T_C is the temperature in the equilibrated melt (at point C). At this annealing condition, the sample is completely crystallized. $\Phi_{\mathrm{am}}(T)$ and $\Phi_{\mathrm{20k}}(T)$ are displayed in Fig. 3d as bold black and blue curves. In the same way the enthalpy curve after annealing for 50,000 s at $T_\mathrm{a} = 138$ °C was calculated. The related normalized enthalpy curves are shown in blue and red in Fig. 11b. The enthalpies $\Delta h_{\mathrm{20k}}(T_\mathrm{a})$ at point B and $\Delta h_{\mathrm{50k}}(T_\mathrm{a})$ at point B' are both above the enthalpy of the least stable modification x1 formed upon heating of the glass, i.e. both crystalline modifications formed during annealing at T_a have a lower formation enthalpy than the metastable modification x1.

The stability of both crystalline modifications can be assessed using the enthalpies and entropies of melting. We estimate the respective enthalpy curves by shifting the black dashed line $\Delta h_{\mathrm{x1}}(T)$ vertically towards the points B' and B (see red and blue dashed lines in Fig. 11b). The melting enthalpies are the difference between the enthalpy of the liquid and the enthalpies of the respective solid modifications at their melting temperatures. Table 1 lists these properties together with the transformation entropies $\Delta s_{\mathrm{m,i}} = \Delta h_{\mathrm{m,i}}/T_{\mathrm{m,i}}$. As can be seen in Table 1, the entropies increase with increasing stability of the crystalline metastable modifications.

Table 1
Thermodynamic properties of the three metastable modifications at the melting temperature. Modification 1 is formed after annealing for 20,000 s at 138 °C, modification 2 is formed after annealing for 50,000 s at 138 °C, and modification x1 is generated at T_{x1} during heating.

	Modification 1 (20,000 s at 138 °C)	Modification 2 (50,000 s at 138 °C)	Modification x1 (formed at T_{x1} during heating)
$T_{\mathrm{m,i}}$ [°C]	245	275	322.1
$\Delta h_{\mathrm{m,i}}$ [kJ mol^{-1}]	2.18	2.72	3.185
$\Delta s_{\mathrm{m,i}}$ [J (mol K)$^{-1}$]	4.21	4.96	5.351

5. Summary and conclusions

The stability of a chemically homogeneous glass (CHG) has been studied by investigating the aging behavior of the BMG-former $Au_{49}Ag_{5.5}Pd_{2.3}Cu_{26.9}Si_{16.3}$, whose melt was quenched at a rate of 20,000 K s^{-1}. The preparation of the CHG and the subsequent measurements were performed using FDSC. The limited fictive temperature of the quenched glass was found to be 175 °C. Thus, the sub-T_g annealing was performed between 108 °C and 168 °C. Using the newly developed concept of critical scanning rates (critical rate approach, see Fig. 1), we find that the following processes occur sequentially during annealing:

(1) Structural relaxation.
(2) Incubation period of nucleation.
(3) Nuclei formation.
(4) Crystallization towards a metastable crystalline phase.
(5) Perfection of the crystalline structure by grain growth and polymorphic transformation to a more stable crystalline state.

The incubation periods of nucleation and of crystal perfection were measured for the first time during isothermal annealing in the glassy state. In the state of structural relaxation a second relaxation event was found for an annealing temperature below 130 °C,

and for $T_a = 118$ °C the times of relaxation end and nucleation onset coincide (Fig. 8).

The measurements further show that the crystalline structure that forms first during annealing has a very low melting temperature. This structure shows a two-step perfection during isothermal annealing. In the first step, the melting temperature gradually increases, which may result from a growth of the nanostructured modification. In such a case, the melting-temperature increase may be explained by a decrease of the interfacial energy of the nanostructured modification (Gibbs-Thomson effect) [65]. The second step is related to a transformation into a more perfect crystalline modification with a slightly higher melting temperature.

The time period between the beginning of structural relaxation and the end of nucleation describes the stability of the supercooled liquid and the resistance against crystallization. Because the incubation time is related to the energy barrier for nucleation, this property is essential for a material with a high kinetic glass stability.

With nuclei forming for annealing times above t_{nuc}, crystallization occurs during subsequent heating and metastable crystalline phases can form (Fig. 3b). For annealing times above t_{cryst}, crystallization already occurs during annealing, so that the glass transition intensity, Δc_p, reduces during subsequent heating (Fig. 3c). After complete crystallization during annealing above t_{reorg}, structural perfection is detected during subsequent heating (Fig. 3d), generating a solid-to-solid transformation to a more stable crystalline state.

After complete structural relaxation at t_{relax}, the sample behaves stable and reveals no structural changes during further annealing until the onset of nuclei formation at t_{nuc}. From the temperature dependence of this incubation time for nucleation (Fig. 8), we derive an activation barrier of 274 kJ mol^{-1}. This is significantly lower than the activation barrier for structural relaxation in the glassy state, which is 374 kJ mol^{-1}. This difference indicates that at very low temperatures, below 120 °C, nucleation can even occur in unrelaxed glasses. Furthermore, at low annealing temperatures (118 °C), an atypical slowdown of the structural relaxation has been observed.

In conclusion, the glass-forming ability of many glass-forming materials can be characterized by the crystallization and melting events above the glass transition. However, such data deliver no reliable information with respect to the glass stability, which is generally important in the context of processing and the application of such materials. This information requires direct study of the kinetics of the different processes that occur in the glassy state. On the other hand, the direct determination of the critical cooling rate is a useful way to characterize the glass-forming ability (GFA) of an alloy. It is an advantage of FDSC that both the determination of GFA and the analysis of glass stability can be performed on one and the same sample in a relatively short time.

Declaration of competing interest

The authors declare that they have no known competing financial interests or personal relationships that could have appeared to influence the work reported in this paper.

Acknowledgments

We thank ETH Zurich and Mettler-Toledo for supporting this collaboration without the need of external funding.

References

[1] D. Turnbull, Under what conditions can a glass be formed? Contemp. Phys. 10 (1969) 473–488.
[2] Y. Li, S.C. Ng, C.K. Ong, H.H. Hng, T.T. Goh, Glass forming ability of bulk glass forming alloys, Scripta Mater 36 (1997) 783–787.
[3] A. Inoue, Bulk amorphous alloys with soft and hard magnetic properties, Mater. Sci. Eng. A226–228 (1997) 357–363.
[4] Z.P. Lu, C.T. Liu, A new glass-forming ability criterion for bulk metallic glasses, Acta Mater 50 (2002) 3501–3612.
[5] M.L.F. Nascimento, L.A. Souza, E.B. Ferreira, E.D. Zanotto, Can glass stability parameters infer glass forming ability? J. Non-Cryst. Solids 351 (2005) 3296–3308.
[6] D. Xu, B.D. Wirth, J. Schroers, W.L. Johnson, Calculating glass-forming ability in absence of key kinetic and thermodynamic parameters, Appl. Phys. Lett. 97 (2010) 024102.
[7] J.F. Löffler, J. Schroers, W.L. Johnson, Time-temperature-transformation diagram and microstructures of bulk glass forming $Pd_{40}Cu_{30}Ni_{10}P_{20}$, Appl. Phys. Lett. 77 (2000) 681–683.
[8] Y. Shen, J.H. Perepezko, Al-based amorphous alloys: glass-forming ability, crystallization behavior and effects of minor alloying additions, J. Alloys Compd. 707 (2017) 3–11.
[9] J.H. Perepezko, C. Santhaweesuk, J.Q. Wang, S.D. Imhoff, Kinetic competition during glass formation, J. Alloys Compd. 615 (2014) S192–S197.
[10] S. Pogatscher, D. Leutenegger, A. Hagmann, P.J. Uggowitzer, J.F. Löffler, Characterization of bulk metallic glass via fast differential scanning calorimetry, Thermochim. Acta 590 (2014) 84–90.
[11] S. Pogatscher, P.J. Uggowitzer, J.F. Löffler, In-situ probing of metallic glass formation and crystallization upon heating and cooling via fast differential scanning calorimetry, Appl. Phys. Lett. 104 (2014) 251908.
[12] N. Neuber, M. Frey, O. Gross, J. Baller, I. Gallino, R. Busch, Ultrafast scanning calorimetry of newly developed Au-Ga bulk metallic glasses, J. Phys.: Condens. Matter 32 (2020) 324001.
[13] E. Lopez, S.L. Simon, Signatures of Structural Recovery in Polystyrene by Nanocalorimetry, Macromolecules 49 (2016) 2365–2374.
[14] X. Monnier, A. Saiter, E. Dargent, Physical aging in PLA through standard DSC and fast scanning calorimetry investigations, Thermochim. Acta 648 (2017) 13–22.
[15] J. Schroers, A. Masuhr, W.L. Johnson, R. Busch, Pronounced asymmetry in the crystallization behavior during constant heating and cooling of a bulk metallic glass-forming liquid, Phys. Rev. B 60 (1999) 11855–11858.
[16] F.X. Bai, J.H. Yao, Y.X. Wang, J. Pan, Y. Li, Crystallization kinetics of an Au-based metallic glass upon ultrafast heating and cooling, Scripta Mater 132 (2017) 58–62.
[17] J.E.K. Schawe, J.F. Löffler, Existence of multiple critical cooling rates which generate different types of monolithic metallic glass, Nature Commun 10 (2019) 1337.
[18] I.S. Gutzow, J.W.P. Schmelzer, The Vitreous State: Thermodynamics, Structure, Rheology, and Crystallization, 2nd ed., Springer, Berlin, Heidelberg, 2013 (ISBN: 978-3-642-42884-5).
[19] E. Zhuralev, J.W.P. Schmelzer, R. Androsch, C. Schick, Experimental test of Tamman's nuclei development approach in crystallization of macromolecules, Intern. Polymer Process. 31 (2016) 628–637.
[20] R. Androsch, C. Schick, Crystal nucleation of polymers at high supercooling of the melt, Adv. Polym. Sci. 276 (2015) 257–288.
[21] R. Androsch, C. Schick, M.L. Di Lorenzo, Kinetics of Nucleation and Growth of Crystals of Poly(L-lactic acid), Adv. Polym. Sci. 279 (2017) 235–272.
[22] R. Androsch, E. Zhuravlev, J.W.P. Schmelzer, C. Schick, Relaxation and crystal nucleation in polymer glasses, Eur. Polym. J. 102 (2018) 195–208.
[23] X. Monnier, Q. Viel, B. Schammé, S. Petit, L. Delbreilh, V. Dupray, G. Coquerel, E. Dargent, Vitrification of two active pharmaceutical incredients by fast scanning calorimetry: from structural relaxation to nucleation phenomena, Int. J. Pharm. 536 (2018) 426–433.
[24] B. Zhao, B. Yng, A.S. Abyzov, J.W. Schmelzer, J. Rodriguez-Viejo, Q. Zhai, C. Schick, Y. Gao, Beating homogeneous nucleation and tuning atomic ordering in glass-forming metal-forming metals by nanocalorimetry, Nano Lett 17 (2017) 7751–7760.
[25] A. Morvan, N. Delpouve, A. Valla, A. Saiter-Fourcin, Physical aging of selenium glass: assessing the double mechanism of equilibration and the crystallization process, J. Non-Cryst. Solids 570 (2021) 121013.
[26] S. Vyazovkin, I. Dranca, Effect of physical aging on nucleation of amorphous indomethacin, J. Phys. Chem B 111 (2007) 7283–7287.
[27] J.E.K. Schawe, C. Wrana, Competition between structural relaxation and crystallization in the glass transition range of random polymers, Polymers (Basel) 12 (2020) 1778.
[28] J. Schroers, B. Lohwongwatana, W.L. Johnson, A. Peker, Gold based bulk metallic glass, Appl. Phys. Lett. 87 (2005) 061912.
[29] Yu.P. Ivanov, C.M. Meylan, N.T. Panagiotopoulos, K. Georgarakis, A.L. Greer, In-situ TEM study of the crystallization sequence in a gold-based metallic glass, Acta Mater 196 (2020) 52–60.
[30] J.E.K. Schawe, T. Hütter, C. Heitz, I. Alig, D. Lellinger, Stochastic temperature modulation: a new technique in temperature-modulated DSC, Thermochim. Acta 446 (2006) 147–155.
[31] G. Tammann, Über die Abhängigkeit der Kerne, welche sich in verschiedenen unterkühlten Flüssigkeiten bilden, von der Temperatur, Zeitschrift für Physikalische Chemie 25U (1898) 441–479.
[32] R. Androsch, C. Schick, A.M. Rhoades, Application of Tammann's Two-Stage Crystal Nuclei Development Method for Analysis of the Thermal Stability of Homogeneous Crystal Nuclei of Poly(ethylene terephthalate), Macromolecules 48 (2015) 8082–8089.

[33] M.J. Richardson, N.G. Savill, Derivation of accurate glass transition temperatures by differential scanning calorimetry, Polymer (Guildf) 16 (1975) 753–757.
[34] C.T. Moynihan, A.J. Easteal, M.A. DeBolt, J. Tucker, Dependence of the fictive temperature of glasses on cooling rate, J. Am. Ceram. Soc. 59 (1976) 12–16.
[35] J.E.K. Schawe, Measurement of the thermal glass transition of polystyrene in a cooling rate range of more than six decades, Thermochim. Acta 603 (2015) 128–134.
[36] S.E.B. Petrie, Thermal behavior of annealed organic glasses, J. Polym. Sci. Part A-2 10 (1972) 1255–1272.
[37] C. Bauwens-Crowet, J.-.C. Bauwens, Annealing of polycarbonate below the glass transition temperature up to equilibrium: a quantitative interpretation of enthalpy relaxation, Polymer (Guildf) 27 (1986) 709–713.
[38] J.E.K. Schawe, S. Pogatscher, J.F. Löffler, Thermodynamics of polymorphism in a bulk metallic glass: heat capacity measurements by fast differential scanning calorimetry, Thermochim. Acta 685 (2020) 178518.
[39] W.F. Hemminger, S. Sarge, The baseline construction and its influence on the measurement of heat with differential scanning calorimeters, J. Thermal Anal. 37 (1991) 1455–1477.
[40] S. Pogatscher, D. Leutenegger, J.E.K. Schawe, P. Maris, R. Schäublin, P.J. Uggowitzer, J.F. Löffler, Monotropic polymorphism in a glass-forming metallic alloy, Journal of Physics: Condensed Matter 30 (2018) 234002.
[41] R.R. Kohlrausch, Theorie des elektrischen Rückstandes in der Leidner Flasche, Annalen der Physik und Chemie (Poggendorff) 91 (1854) 179–214.
[42] D.V. Louzguine-Luzgin, I. Seki, S.V. Ketov, L.V. Louzguina-Luzgina, V.I. Polkin, N. Chen, H. Fecht, A.N. Vasiliev, H. Kawaji, Glass-transition process in an Au-based metallic glass, J. Non-Cryst. Solids 419 (2015) 12–15.
[43] C.A. Angell, Entropy and fragility in supercooling liquids, J. Res. Natl. Inst. Stand. Technol. 102 (1997) 171–185.
[44] I. Gallino, D. Cangialosi, Z. Evenson, L. Schmitt, S. Hechler, M. Stolpe, B. Ruta, Hierarchical aging pathways and reversible fragile-to-strong transition upon annealing of a metallic glass former, Acta Mater 144 (2018) 400–410.
[45] L. Song, W. Xu, J. Huo, J.-.Q. Wang, X. Wang, R. Li, Two-step relaxations in metallic glasses during isothermal annealing, Intermetallics 93 (2018) 101–105.
[46] Q. Wang, S.T. Zhang, Y. Yang, Y.D. Dong, C.T. Liu, J. Lu, Unusual fast secondary relaxation in metallic glass, Nat. Commun. 6 (2015) 7876.
[47] C. Liu, E. Pineda, D. Crespo, J. Qiao, Z. Evenson, B. Ruta, Sub-Tg relaxation times of the α process in metallic glasses, J. Non-Cryst. Solids 471 (2017) 322–327.
[48] X. Monnier, D. Cangialosi, B. Ruta, R. Busch, I. Gallino, Vitrification decoupling from α-relaxation in a metallic glass, Sci. Adv. 6 (2020) eaay1454.
[49] J.H. Perepezko, K. Hildal, Analysis of solidification microstructure during wedge-casting, Phil. Mag. 86 (2006) 3681–3701.
[50] J.W.P. Schmelzer, A.S. Abyzov, Crystallization of glass-forming liquids: thermodynamic driving force, J. Non-Cryst. Solids 449 (2016) 41–49.
[51] J.E.K. Schawe, K.U. Hess, The kinetics of the glass transition of silicate glass measured by fast scanning calorimetry, Thermochim. Acta 677 (2019) 85–90.
[52] Y. Abe, T. Arahori, A. Naruse, Crystallization of $Ca(PO_3)_2$ glass below the glass transition temperature, J. Am. Ceram. Soc. 59 (1976) 487–490.
[53] N. Okamoto, M. Oguni, Y. Sagawa, Generation and extinction of a crystal nucleus below the glass transition temperature, J. Phys.: Condens. Matter 9 (1997) 9187–9198.
[54] F. Paladi, M. Oguni, Generation and extinction of crystal nuclei in an extremely non-equilibrium glassy state of salol, J. Phys.: Condens. Matter 15 (2003) 3909–3917.
[55] S.C. Glade, J.F. Löffler, S. Bossuyt, W.L. Johnson, M.K. Miller, Crystallization of amorphous $Cu_{47}Ti_{34}Zr_{11}Ni_8$, J. Appl. Phys. 89 (2001) 1573–1579.
[56] X.-.P. Tang, J.F. Löffler, W.L. Johnson, Y. Wu, Devitrification of the $Zr_{41.2}Ti_{13.8}Cu_{12.5}Ni_{10}Be_{22.5}$ bulk metallic glass studied by XRD, SANS, and NMR, J. Non-Cryst. Solids 317 (2003) 118–122.
[57] E. Pekarskaya, J.F. Löffler, W.L. Johnson, Microstructural studies of crystallization of a Zr-based bulk metallic glass, Acta Mater 51 (2003) 4045–4057.
[58] D.V. Louzguine-Luzgin, Vitrification and devitrification processes in metallic glasses, J. Alloys Compd. 586 (2014) 52–58.
[59] S. Pogatscher, D. Leutenegger, J.E.K. Schawe, P.J. Uggowitzer, J.F. Löffler, Solid–solid phase transitions via melting in metals, Nat. Commun. 7 (2016) 11113.
[60] J.E.K. Schawe, Temperature correction at high heating rates for conventional and fast differential scanning calorimetry, Thermochim. Acta 698 (2021) 178879.
[61] G. Dalla Fontana, G.L. Fiore, L. Battezzati, Thermodynamics of the $Au_{49}Ag_{5.5}Pd_{2.3}Cu_{26.9}Si_{16.3}$ glass-forming alloy, J. Non-Cryst. Solids 382 (2013) 95–98.
[62] G. Fiore, P. Rizzi, L. Battezzati, Phase constitution and glass formation in an Au-based alloy, J. Alloys Comp. 509S (2011) S166–S169.
[63] K.S. Gavrichev, G.A. Sharpataya, V.N. Guskov, J.H. Greenberg, T. Feltgen, M. Fiederle, K.W. Benz, Thermodynamic properties of ZnTe in the temperature range 15–925K, Phys. Stat. Sol. 229 (2002) 133–135.
[64] R. Busch, W. Liu, W.L. Johnson, Thermodynamics and kinetics of the $Mg_{65}Cu_{25}Y_{10}$ bulk metallic glass forming liquid, J. Appl. Phys. 83 (1998) 4134.
[65] F. Meissner, Über den Einfluss der Zerteilung auf die Schmelztemperatur, Zeitschrift für anorganische und allgemeine Chemie 110 (1920) 169–186.